Materials Science Forum
ISSN: 1662-9752, Vol. 925, pp 353-360
doi:10.4028/www.scientific.net/MSF.925.353

Submitted: 2017-08-01
Revised: 2017-12-22
Accepted: 2018-01-09
Online: 2018-06-20

High-Temperature Oxidation of a High Silicon SiMo Spheroidal Cast Iron in Air with *In Situ* Change in H_2O Content

André Ebel[1,3,a], Serge Yapi Brou[2,b], Benoit Malard[1,c], Jacques Lacaze[1,d], Daniel Monceau[1,e] and Loïc Vaissière[3,f]

[1]CIRIMAT, Université de Toulouse, CNRS, INPT, UPS, 4 allée Emile Monso, 31030 Toulouse, France

[2]Laboratoire de Chimie Physique, Université Félix Houphouët-Boigny, 22 BP 582 Abidjan 22, Côte d'Ivoire

[3]Renault SA, Technocentre, 1 avenue du Golf, 78084 GUYANCOURT, France

[a]andre.ebel@ensiacet.fr, [b]lesaintbys@yahoo.fr, [c]benoit.malard@ensiacet.fr, [d]jacques.lacaze@ensiacet.fr, [e]daniel.monceau@ensiacet.fr, [f]loic.vaissiere@renault.com

Keywords: Cast iron, SiMo, high temperature oxidation, water vapor.

Abstract. Exhaust manifolds for diesel engines are made of high-Si ferritic nodular cast irons. It is experimentally well established that their oxidation kinetics are highly sensitive to the presence of water vapor, though the mechanism for such an effect is still controversial. In the present work, isothermal oxidation tests were performed on a SiMo nodular cast iron at 700 °C and 800 °C in dry and humid air for 25 and 50 hours. Other samples were oxidized for 50 h with in-situ change in H_2O content after 25 h, switching from dry air to humid air or the other way around. Samples were then analyzed using XRD, SEM-EDS and Raman spectroscopy. Thermogravimetric records clearly showed the effect of temperature and environment on oxidation and decarburization. The kinetics of these phenomena depend on silica formation at the metal-oxide interface. At both temperatures, water vapor was seen to promote internal oxidation of Si instead of its external oxidation. This leads to higher oxidation rate at 700 °C and higher decarburization rate at 800 °C.

Introduction

Cast iron has long been selected for manufacturing exhaust components due to its low cost/performance ratio. Lamellar grey iron has been used for more than 50 years in the beginning of the 20th century. To face increasing exhaust gas temperature, common spheroidal graphite cast iron (SGI) was used in the 1960's, then SiMo SGI in the 1980's. Since then, the tendency was to increase Si content up to 4.5 wt. % and decrease Mo content down to 0.5 wt. %, resulting in modern Hi-SiMo SGI with low pearlite content. Still, in order to meet new European standards for lower exhaust emission and higher engine efficiency, combustion temperature keeps rising, leading to increased thermal and mechanical loads on exhaust components.

To avoid resorting to costly materials such as the Ni-bearing D5S, many attempts at improving the high temperature behavior of ferritic SGI have been carried out. Further increasing Si content over 5 wt.% is detrimental because it leads to increased brittleness [1] at low temperature. Alloying with other elements such as Cr, Ni, V and Al has been considered [2–4] but without apparently yet meeting the cost-performance ratio of Hi-SiMo SGI. Therefore, carmakers are considering extending the temperature range of this material.

The maximum temperature of ferritic SGI in service is limited by three phenomena: the ferrite–austenite phase transition which leads to dimensional changes [5], decarburization which increases with temperatures above 800 °C [5] but shows little variation with Si-content [5,6], and oxidation. On Fe-Si alloys and SiMo SGI, oxidation usually proceeds in two steps. Initially, a thin and protective Si-rich oxide scale is formed, then fast-growing nodules of iron oxide nucleate, leading to the formation of mixed scale with complex kinetics [7]. Over time, those nodules grow laterally until they cover the whole sample surface. For Hi-SiMo SGI, the resulting scale is multi-layered with outward growing iron oxides, magnetite and hematite, an inward growing subscales of

magnetite and fayalite and Si-rich oxide at the metal-oxide interface [8,9]. While the reason for the initiation of these iron oxide nodules on Fe-Si alloys is still not clear [7], it is often linked to graphite combustion on SGI [8,9]. Increasing Si-content promotes Si-rich oxide scale formation at the metal-oxide interface such as fayalite (Fe_2SiO_4) and silica (SiO_2). Those oxide layers act as diffusion barriers and are able to reduce oxidation kinetics and scale thickness even if they are discontinuous [1,10,11].

Exhaust components are exposed to both ambient air and combustion gas. Diesel engine combustion gas is mainly nitrogen, carbon dioxide and water vapor. As diesel combustion takes place at high air/fuel ratio, combustion gas also presents large amounts of oxygen [12]. Tholence et al. [13] as well as Ekström et al. [8] studied oxidation of SiMo SGI in diesel exhaust gases and demonstrated the key role of water vapor in the oxidation mechanism over carbon dioxide and nitrogen oxides. Works form Fukumoto et al. [14] on Fe-1.5Si alloys in different H_2O containing atmospheres demonstrated that water vapor accelerated nucleation of iron oxide nodules, increased oxidation kinetics and led to porous iron oxide scales. Early works from Parent-Simonin et al. [15] strongly suggest that water vapor might have a key role on decarburization of SGI as well. However, the effect of water vapor on oxidation mechanisms of Fe-Si alloys and decarburization of SGI with high Si-content remains poorly understood. Recent works on Hi-SiMo SGI point out oxidation as a failure mechanism under Low Cycle Fatigue (LCF) and Thermo-Mechanical Fatigue (TMF) loadings [16,17] and the effect of environment on LCF life [16]. Some works even correlate oxidation resistance and TMF resistance [18]. The aim of this study was thus focused on the effect of water vapor on oxidation and decarburization of Hi-SiMo SGI at elevated temperatures.

Experimental Details

A Hi-SiMo SGI was cast at Fonderie de Bretagne as Y-blocks resulting in 25·50·200 mm^3 blocks. Its composition was determined on a cast block using a Panalytical Axios Advanced XRF spectrometer and optical emission spectroscopy (Table 1). A typical microstructure after Nital etching is shown in Fig. 1 where it is seen that pearlite and Mo-bearing carbides appear in last to freeze areas.

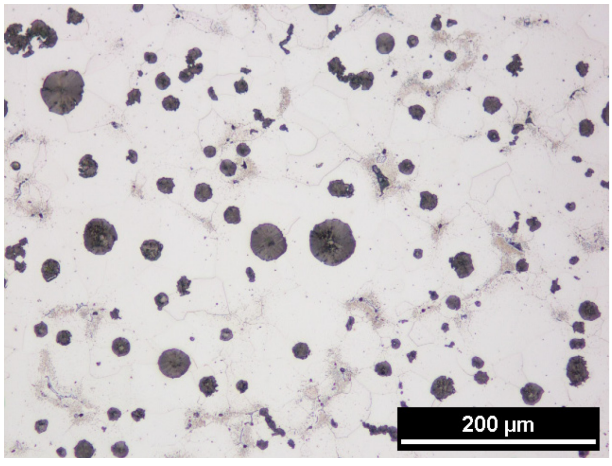

Figure 1: Optical micrograph after Nital etching of the Hi-SiMo SGI.

Table 1: Chemical composition (wt.%) of the SiMo SGI used in the present work.

C	Si	Mo	Mn	Cr
3.2	4.4	0.5	0.24	0.04
Ni	**Cu**	**Sb**	**Ti**	**V**
0.045	0.055	0.013	0.009	0.004
Sn	**S**	**P**	**Fe**	
0.006	0.007	0.02	balance	

Prior to oxidation, test coupons were polished using SiC paper down to P1200 grit, rinsed in acetone and ethanol, then cleaned in an ultrasonic bath in ethanol. Their dimensions were measured using a vernier and their initial mass with a Sartorius precision balance (± 10 µg precision). After polishing, test coupons average dimensions and weight were 19.2·9.6·1.7 mm^3 and 2.1 g. Thermogravimetric analysis (TGA) was conducted using a SETARAM TAG24s thermogravimetric unit for experiments in dry air and a SETARAM Setsys Evo thermogravimetric unit coupled with a SETARAM Wetsys humidity generator for experiments in humid air. Humid air generation was prepared at 35 °C with a relative humidity of 90 %, resulting in 5 Vol. % H_2O content (hereafter

called humid air). Reference isothermal tests with 25 and 50 hours duration were performed in dry and humid air with a flow rate set to $1.3 \cdot 10^{-3}$ m/s. This flow rate was chosen large enough to have no effect on the resulting oxidation kinetics. Then 50 h isothermal tests were performed with in-situ change of the H_2O content. All tests were performed at both 700 °C and 800 °C as summarized in Table 2. The resulting TGA curves represent specific mass gain ($\Delta m/S$) according to time. For confidentiality reasons, these curves have been normalized with the maximum specific mass gain obtained during DA2_700C experiment (Table 2).

Following testing, samples were characterized using Brüker D8 Advanced XRD equipped with a copper anode. XRD was performed on sample surface immediately after oxidation as well as after polishing of the external scale. Surface and cross section observations were performed with a LEO435VP scanning electron microscope (SEM) coupled with an Imix electron dispersive spectrometer (EDS). Some samples were electroplated with copper before cross-sectioning in order to preserve oxide scale integrity during cutting. Qualitative EDS line profiles were performed on oxide scale cross-section. For presentation purpose, EDS measurements have been normalized with the maximum intensity measured for each element. Finally, Raman spectroscopy was performed on cross sections using a HORIBA Labram HR 800 system equipped with a 532 nm laser.

Table 2: List of experiments and experimental conditions.

Reference	Duration/atmosphere	T (°C)	Test apparatus
DA1_700C	25h / Dry Air	700	TAG24s
DA1_800C	25h / Dry Air	800	TAG24s
HA1_700C	25h / Humid air	700	Setsys Evo+Wetsys
HA1_800C	25h / Humid air	800	Setsys Evo+Wetsys
DA2_700C	50h / Dry Air	700	TAG24
DA2_800C	50h / Dry Air	800	TAG24
HA2_700C	50h / Humid air	700	Setsys Evo+Wetsys
HA2_800C	50h / Humid air	800	Setsys Evo+Wetsys
DAHA_700C	25h / Dry Air - 25h / Humid air	700	Setsys Evo+Wetsys
DAHA_800C	25h / Dry Air - 25h / Humid air	800	Setsys Evo+Wetsys
HADA_700C	25h / Humid air - 25h / Dry Air	700	Setsys Evo+Wetsys
HADA_800C	25h / Humid air - 25h / Dry Air	800	Setsys Evo+Wetsys

Results

TGA curves. TGA for 25 h and 50 h reference tests in dry and humid air are presented in Fig. 2 and those for 50 h tests with in-situ change in H_2O content in Fig. 3.

According to TGA curves in Fig. 2 and metallographic observations in Figs. 4 and 5, SGI oxidation goes through three steps (see indications on Fig. 2.a for the 700 °C curves):

i) graphite in contact with the atmosphere gets oxidized to carbon dioxide leading to an initial mass loss;
ii) fast-growing iron oxides nodules nucleate all over the surface and grow laterally leading to a fast initial mass gain kinetics;
iii) oxide nodules tend to connect to each other to form a more or less uniform oxide scale covering the whole sample surface and thus reducing the mass gain rate.

Curves in Fig. 2 show that the total mass gains after 25 h are significantly higher during oxidation at 700 °C than at 800 °C. In dry air, despite some result discrepancy, the total mass gains after 50 h at 700 °C and 800 °C have the same order of magnitude (Fig. 2.a). In humid air on the contrary, total mass gains remain much higher at 700 °C than at 800 °C (Fig. 2.b). However, the shape of the curve for the tests at 800 °C in humid air suggests that another phenomenon takes place as the same time as oxide scale growth which leads to mass loss. Oxide scale thickness measurements on cross section of the samples were in full agreement with the overall mass gains in

Fig. 2 for tests at 700 °C, while scales are much thicker in humid air than in dry air for similar mass gains at 800 °C.

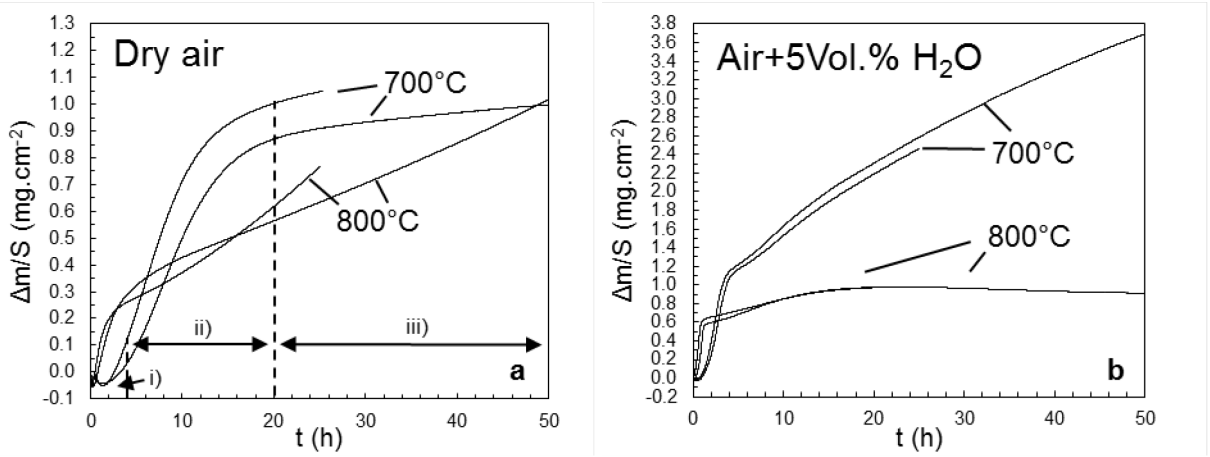

Figure 2: Thermogravimetric analysis of SiMo SGI at 700 and 800 °C in dry air (a) and humid air (b) for 25 and 50 h. Indications of the three steps of oxidation on Fig. 2.a are for the 700 °C curves.

Fig. 3 shows the TGA curves with in-situ change in H_2O content after 25 h. As expected, the mass changes during the first 25 h are similar to those seen in Fig. 2, for both temperatures and atmospheres. On the contrary, the effect of switching the atmosphere is contrasted. At 700 °C, mass variation kinetics tends to increase when the atmosphere is switched from dry to humid air (Fig. 3.a) while it tends to decrease when the atmosphere is switched from humid to dry air (Fig. 3.b). At 800 °C, opposite tendencies are observed: mass gain strongly slows down when switching from dry to humid air whereas it increases when switching from humid to dry air.

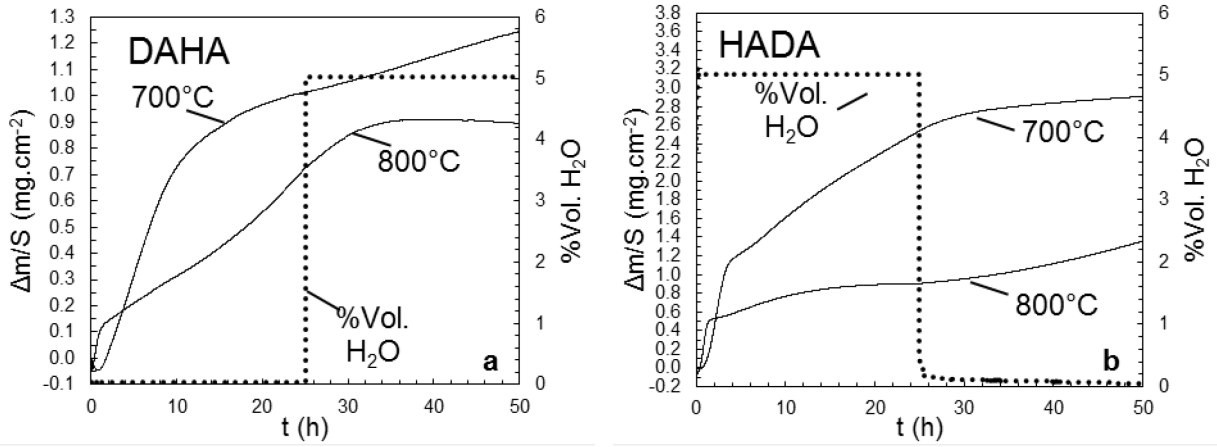

Figure 3: Thermogravimetric analysis of SiMo SGI at 700 °C and 800 °C in dry air for 25 h followed by humid air for 25 h (a) and vice versa (b).

Cross-section observations. The micrograph of sample DA2_700C in Fig. 4.a shows that two types of oxide scale developed after 50 h in dry air: one very thin (<1 µm) and one thick (50-100 µm). The same observation was made on all samples oxidized in dry air. The thick oxide scale consists in two layers, an external layer and an internal layer which are both compact.

Scales developed in humid air only present the thick multi-layered oxide scale with large voids within the external layer as seen in the micrograph of sample HA2_700C in Fig. 4.b. It is noteworthy that the scale grown in humid air at 700 °C has a homogeneous thickness all over the sample while it presents large nodules with thinner scale in between after oxidation at 800 °C (Fig. 5.a). Further, internal oxidation at metal-oxide interface was observed on samples oxidized in humid air. At 700 °C, it was found all along the interface (Fig. 4.b) while it appeared only along thick nodules at 800 °C (Fig. 5.b).

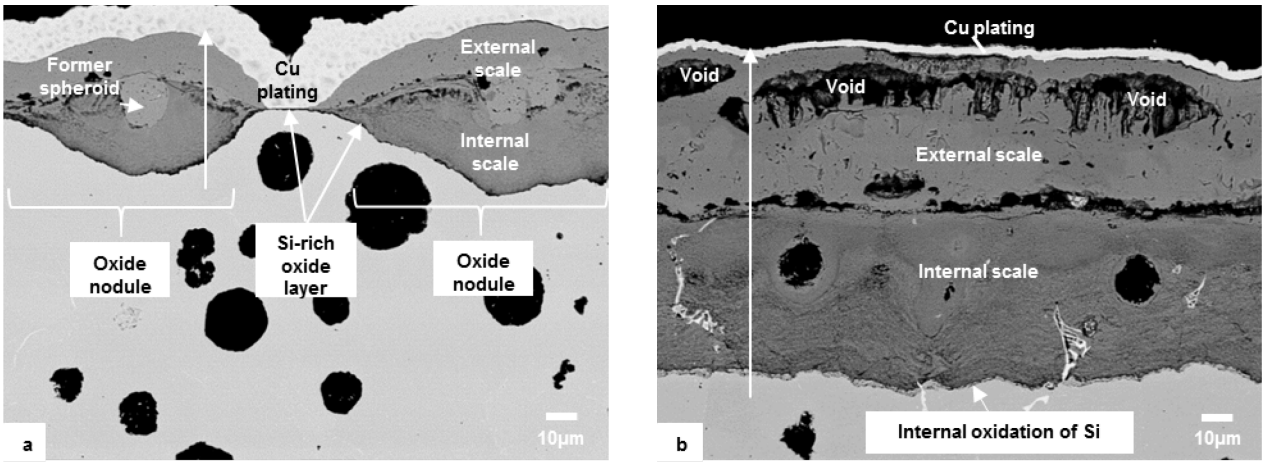

Figure 4: BSE-SEM images of oxide scale on samples DA2_700C (a) and HA2_700C (b). EDS line profiles shown in Fig. 9 performed on these samples are indicated with white arrows.

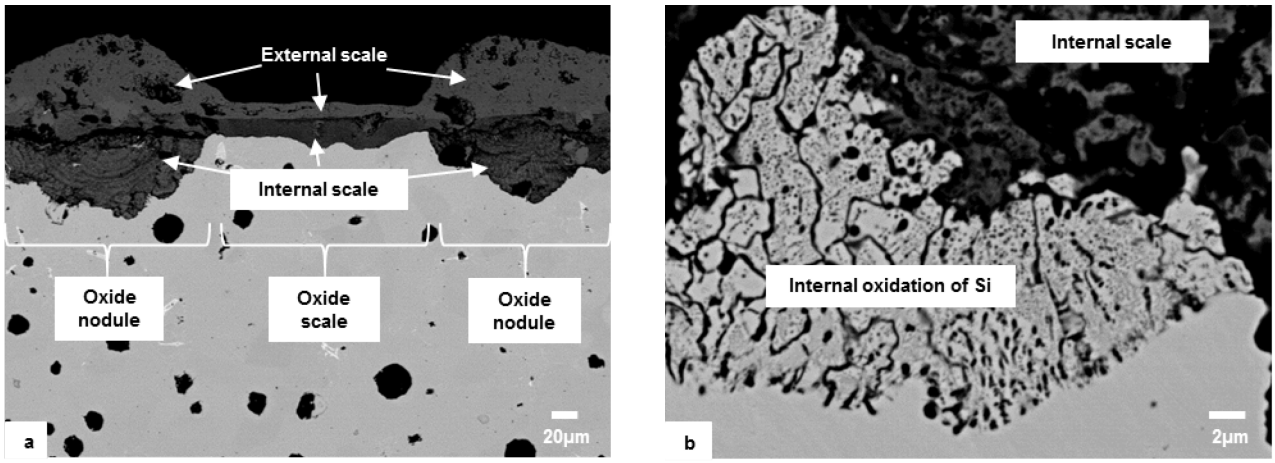

Figure 5: BSE-SEM images of samples HA2_800C showing an overview of the oxide scale (a) and an enlargement on an area with internal oxidation (b).

Oxide scales grown at 700 °C with in-situ change in H_2O content are uniform and show large voids in the external scale as illustrated in Fig. 6. On samples first oxidized in dry air then in humid air, most of the scale is compact. Voids in the external scale are only found in a few locations along with internal oxidation at metal-oxide interface (Fig. 6.a). On samples first oxidized in humid air then in dry air, voids were found all along the surface (Fig. 6.b).

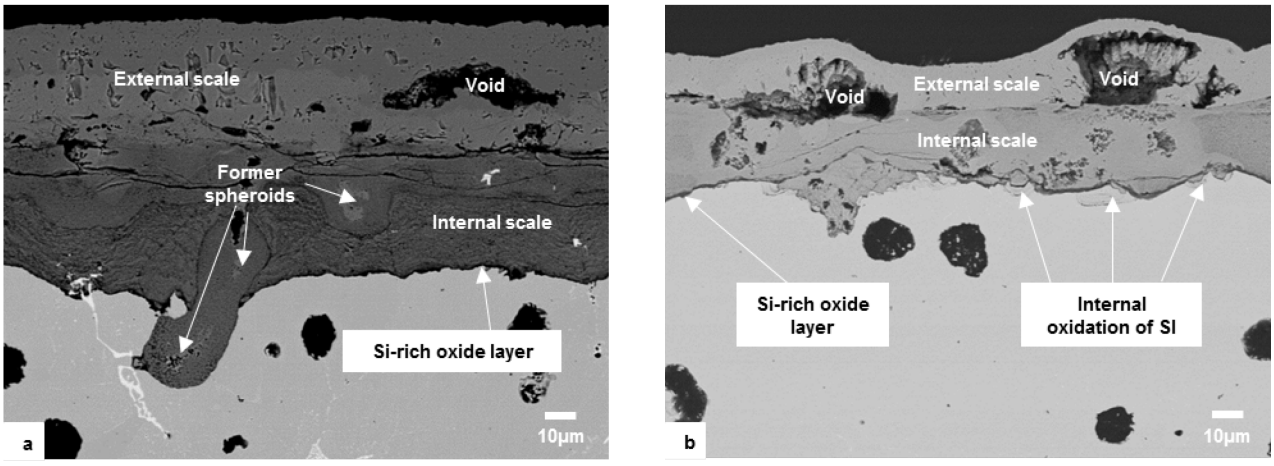

Figure 6: Back-scattered electrons SEM images of oxide scales on samples DAHA_700C (a) and HADA_700C (b).

Oxide scales grown at 800 °C with in-situ change in H_2O content present large oxide nodules with large voids and cracks, and some internal oxidation along oxide nodules as observed on samples oxidized in humid air. For the sample first oxidized in dry air, areas with thin oxide scale are still present in between oxide nodules while this is not observed on samples first oxidized in humid air.

A clear gradient in graphite spheroid density could be observed within the substrate of samples oxidized in humid air at 800 °C while this was not found on those oxidized in dry air. This was also observed to a lower extent on samples oxidized at 800 °C with in-situ change in H_2O content while it was not observed on any sample oxidized at 700 °C.

Nature and Composition of Oxide Scales

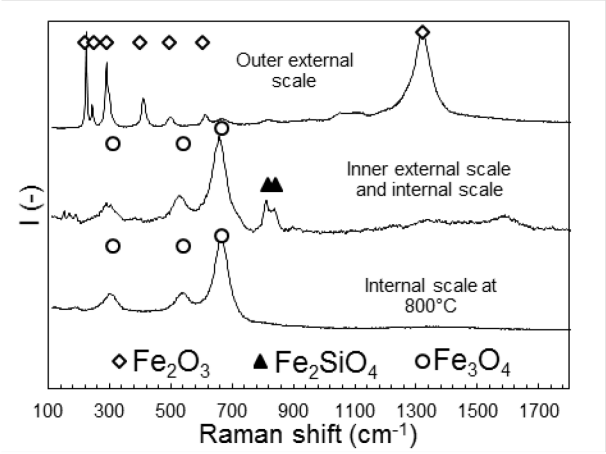

Figure 7: Summary of Raman spectroscopy performed on all 50 h samples.

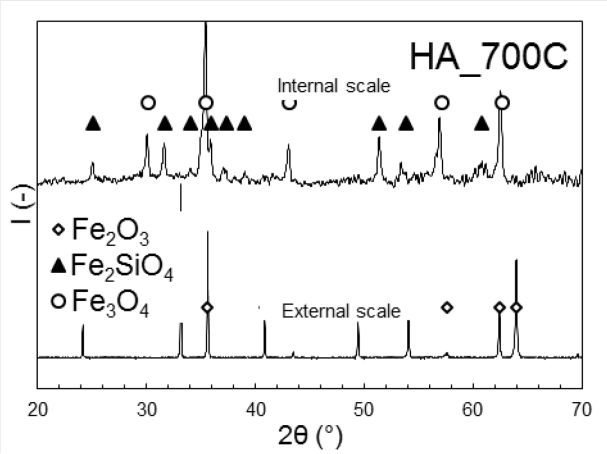

Figure 8: X-Ray diffractograms of internal and external scales on HA_700C sample.

Raman spectroscopy performed on oxide scales (Fig. 7) showed that only the outer part of the external scale is made of hematite (Fe_2O_3) whilst its inner part consists in magnetite (Fe_3O_4). Oxides detected in the internal scale at 800 °C are magnetite and fayalite (Fe_2SiO_4) while only magnetite is detected at 700 °C. Either hematite or magnetite were found on former graphite spheroid locations in the internal scale. Oxides formed at the metal-oxide interface could not be identified. The above Raman spectroscopy results were complemented with XRD. As illustrated in Fig. 8 for sample HA_700C, the outer external scale was identified as hematite and the inner scale as a mix of magnetite and fayalite while the latter was not detected with Raman spectroscopy at 700 °C.

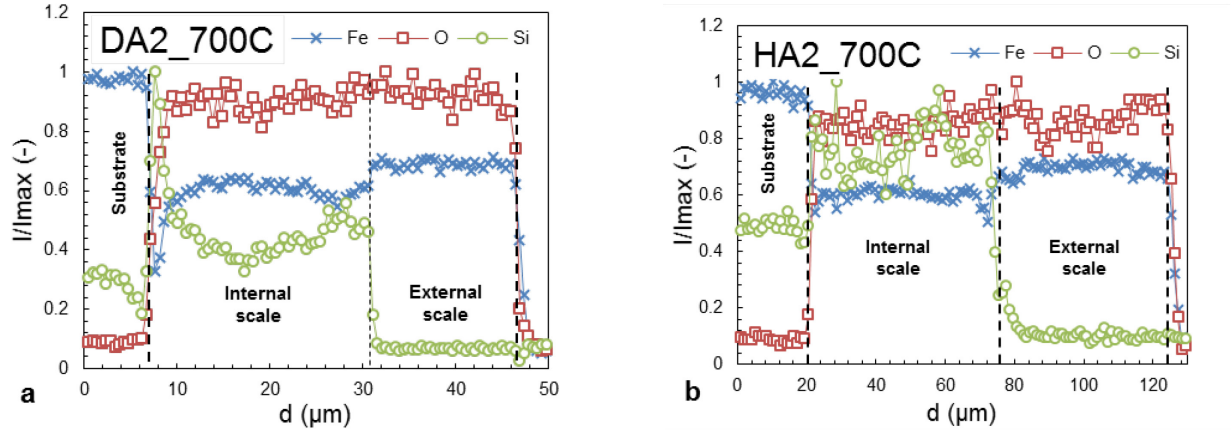

Figure 9: Normalized EDS line profiles performed on cross sections of samples DA2_700C (a) and HA2_700C (b) along arrows indicated respectively on Fig. 4.a and b.

EDS line profiles were recorded on all 50 h samples. They showed that the internal layer presents Fe, Si and O while the external layer only contains Fe and O. A peak in Si-content was found at the

metal-oxide interface for all samples except those oxidized in humid air at 700 °C, as seen by comparing the two graphs in Fig. 9.

Discussion

The silicon-rich oxide layer at metal-oxide interface is assumed to be SiO_2 (silica) which has a very slow growth kinetics [19] in comparison with iron oxides [11] and acts as a very efficient diffusion barrier at the temperatures in use for the present study [20]. Then, the thickness and continuity of silica may control the oxidation and decarburization kinetics. As it grows very slowly, silica formed at lower temperature is thinner and less continuous than the one formed at higher temperature. The Wagner's transition criteria [21] between internal and external oxidation may be also reached at 800 °C and not at 700 °C. This could explain the faster oxidation at 700 °C than at 800 °C observed in dry air, which is in good agreement with other results on SiMo SGI [8] and Fe-Si alloys [7] with similar Si-content. In humid air, SiO_2 layer is not always found and internal oxidation of Si is observed instead. This could be due to an increase of oxygen permeability in iron with water vapor and its effect on internal oxidation. This explains the larger mass gains and faster oxidation kinetics observed, especially at 700 °C.

FeO, Fe_2SiO_4 and SiO_2 are stable below the FeO-Fe_3O_4 equilibrium oxygen partial pressure. However, SiO_2 reaction with FeO to form Fe_2SiO_4 is thermodynamically favored above 500 °C [7,11]. Thus, the sustainability of SiO_2 depends on FeO and Fe_2SiO_4 formation rates. As previously observed on Hi-SiMo SGI [8], SiO_2 and Fe_2SiO_4 are observed but not FeO after oxidation in dry and humid air. Then, it can be assumed that FeO formation is the limiting reaction for fayalite formation in this atmosphere. Absence of SiO_2 in humid air can be due to faster FeO formation when H_2O is present. According to Wagner analysis of internal oxidation [21], the presence of internal oxidation of Si would mean that the Si-content at the metal-oxide interface is not high enough to sustain SiO_2 formation. However, experiments with in-situ change in H_2O content show that the latter is not true because SiO_2 is formed when the atmosphere switches from humid air to dry air. Consequently, it can be assumed that H_2O acts on diffusion and/or solubility of O or diffusion of Si in ferrite to promote internal oxidation of Si. An interplay with the carbon in solution in the metallic matrix is also possible.

Decarburization relies on C diffusion towards the oxide scale to react with oxygen, water vapor or iron oxides to form gaseous carbon oxides. Then, the gas formed needs escaping the oxide scale for decarburization to keep proceeding. Thus, decarburization should be slowed down if a diffusion barrier such as silica is present and if the oxide scale is compact as observed in dry air. On the contrary, fast decarburization can be correlated with the absence of a dense and continuous silica layer and the porous structure of the large oxide nodules observed in humid air at 800 °C. The absence of extensive decarburization at 700 °C even without formation of silica layer confirms that this phenomenon is thermally activated and only takes place above 800 °C as previously mentioned [5].

Conclusion

The aim of this work was to study the effect of water vapor and temperature on oxidation and decarburization of Hi-SiMo SGI. The main results are that the kinetics of these two phenomena are controlled by the formation of silica at the metal-oxide interface which depends on both temperature and on the presence of water vapor. Accordingly, as the formation of a continuous silica scale is favored at 800 °C in comparison with 700 °C, oxidation rate tends to decrease as well with temperature in dry air. H_2O acts on oxidation mechanisms so that internal oxidation of Si is found rather than formation of a continuous SiO_2 external scale that would act as a diffusion barrier. This leads to a large increase in oxidation rate at 700 °C and in decarburization rate at 800 °C, in the presence of water vapor in the atmosphere

References

[1] W. Fairhurst, K. Rohrig, High-silicon nodular irons, Foundry Trade Journal. 146 (1979) 657–681.

[2] R. Yamauchi, S. Ishizuka, N. Suzuki, Development of Vanadium-added Heat Resistant Cast Iron for Exhaust Manifold, SAE Technical Paper, 2010.

[3] M. Ekström, Oxidation and corrosion fatigue aspects of cast exhaust manifolds, Doctoral thesis, KTH Royal Institute of Technology, 2015.

[4] K. Papis, S. Tunzini, W. Menk, Cast iron alloys for exhaust applications, 10th International Symposium on the Science and Processing of Cast Iron, Mar Del Plata, Argentina. (2014).

[5] P. Bastid, P. Pilvin, C. Grente, E. Andrieu, Microstructural Evolution of Spheroidal Graphite Cast Iron at High Temperature: Consequences on Mechanical Behaviour, Adv. Mat. Res. 4–5 (1997) 139–146.

[6] Y. Yamaguchi, S. Kiguchi, H. Sumimoto, D.K. Nakamura, Effect of graphite morphology on decarburized cast iron, Int. J. Cast. Metal Res. 16 (2003) 137–142.

[7] L.L. Liu, Q.Q. Guo, Y. Niu, Transition Between Different Oxidation Modes of Binary Fe–Si Alloys at 600–800 °C in Pure O_2, Oxid Met. 79 (2013) 201–224.

[8] M. Ekström, P. Szakalos, S. Jonsson, Influence of Cr and Ni on High-Temperature Corrosion Behavior of Ferritic Ductile Cast Iron in Air and Exhaust Gases, Oxid Met. 80 (2013) 455–466.

[9] F. Tholence, M. Norell, High-Temperature Corrosion of Cast Irons and Cast Steels in Dry Air, Materials Science Forum. 369–372 (2001) 197–204.

[10] I. Svedung, N.-G. Vannerberg, The influence of silicon on the oxidation properties of iron, Corros. Sci. 14 (1974) 391–399.

[11] A. Atkinson, A theoretical analysis of the oxidation of Fe–Si alloys, Corros. Sci. 22 (1982) 87–102.

[12] J.B. Heywood, Internal combustion engine fundamentals, Mcgraw-hill New York, 1988.

[13] F. Tholence, M. Norell, High Temperature Corrosion of Cast Alloys in Exhaust Environments I-Ductile Cast Irons, Oxid Met. 69 (2008) 13–36.

[14] M. Fukumoto, S. Maeda, S. Hayashi, T. Narita, Effect of Water Vapor on the Oxidation Behavior of Fe–1.5Si in Air at 1073 and 1273 K, Oxid Met. 55 (2001) 401–422.

[15] S. Parent-Simonin, C. Moreaux, J.C. Margerie, Influence of the Annealing Atmosphere on the Structure of Malleable Cast Irons, Rev. Metall. 74 (1977) 537–543.

[16] M. Ekström, S. Jonsson, High-Temperature Corrosion Fatigue of a Ferritic Ductile Cast Iron in Inert and Corrosive Environments at 700°C, 10th International Symposium on the Science and Processing of Cast Iron, Mar Del Plata, Argentina. (2014).

[17] X. Wu, G. Quan, R. MacNeil, Z. Zhang, X. Liu, C. Sloss, Thermomechanical Fatigue of Ductile Cast Iron and Its Life Prediction, Metall. Mater. Trans. A. 46 (2015) 2530–2543.

[18] V. Norman, P. Skoglund, D. Leidermark, J. Moverare, Damage Mechanisms in Silicon-Molybdenum Cast Irons subjected to Thermo-Mechanical Fatigue, Int. J. Fatigue. 99 (2017) 258–265.

[19] B.E. Deal, A.S. Grove, General relationship for the thermal oxidation of silicon, J. Appl. Phys. 36 (1965) 3770–3778.

[20] A. Atkinson, J.W. Gardner, The diffusion of Fe^{3+} in amorphous SiO_2 and the protective properties of SiO_2 layers, Corros. Sci. 21 (1981) 49–58.

[21] C. Wagner, Reaktionstypen bei der Oxydation von Legierungen, Zeitschrift Für Elektrochemie, Berichte Der Bunsengesellschaft Für Physikalische Chemie. 63 (1959) 772–782.